CHARACTERIZATION OF SOLID COMPOSITE PROPELLANTS USING TWO-DIMENSIONAL DIGITAL IMAGE CORRELATION AT LARGE AND SMALL SCALES

by

Christopher Jarocki

A Thesis

Submitted to the Faculty of Purdue University

In Partial Fulfillment of the Requirements for the degree of

Master of Science in Aeronautics and Astronautics

School of Aeronautics and Astronautics

West Lafayette, Indiana

May 2022

THE PURDUE UNIVERSITY GRADUATE SCHOOL
STATEMENT OF COMMITTEE APPROVAL

Dr. Steven F. Son, Chair

School of Mechanical Engineering

Dr. Jeffrey F. Rhoads

School of Mechanical Engineering

Dr. Li Qiao

School of Aeronautics and Astronautics

Dr. Sally P. Bane

School of Aeronautics and Astronautics

Approved by:

Dr. Gregory Blaisdell

This work is dedicated to my fiancée, Shannon, and my parents, James and Kristin, for their unwavering support, encouragement, and advice throughout my time here at Purdue.

ACKNOWLEDGMENTS

I'd like to begin by expressing my sincere thanks and gratitude towards my advisor and mentor, Dr. Steven Son. His advice, encouragement, and knowledge over the past two years have been invaluable in helping me complete my academic and scientific goals. My lab mates and friends here at Zucrow Labs have also been a major part of my success, and I would be remiss if I did not specifically thank them. Notably, I would like to thank Tim Manship, Michael Baier, Daniel Klinger, Tim Wagner, Gus Caito, Ben Worrell, Harry Amadeo, Megan Armstrong, and Joey Lawrence. Finally, I owe my deepest gratitude and appreciation to my fiancée, Shannon, for encouraging, motivating, and enabling me to succeed at my highest possible levels.

The work in this thesis was funded by the Defense Advanced Research Projects Agency (DARPA). The views, opinions, and/or findings expressed are those of the author and should not be interpreted as representing the official views or policies of the Department of Defense or the U.S. Government.

TABLE OF CONTENTS

LIST OF TABLES

LIST OF FIGURES

ABSTRACT

Solid composite propellants are used widely in the aerospace industry due to their desirable mechanical and performance characteristics, including their simplicity, high initial thrust and volume specific impulse. Knowledge of the mechanical properties is needed due to the stresses encountered by a solid rocket motor propellant during thermal cycling while in storage, during rapid ignition transients, and dynamic launch and flight phases. These stresses could damage the propellant grain, leading to an unplanned increase in burning surface area and subsequent catastrophic disassembly.

Tensile testing with the conventionally used JANNAF Type C "dogbones" can be material-expensive and time-consuming, particularly if determining the propellant's response to different strain rates and temperatures. The rapid development of propellants with novel ingredients or formulations is especially hampered by material and time constraints. Using small-scale tests, typically using "micro-dogbone" samples, tensile properties can be characterized with a strong correlation to standard JANNAF Type C samples and only use a fraction of the normally required material. The correlation between the two sample sizes can be demonstrated for a wide range of propellant formulations and environmental conditions, such as extreme temperatures used in test conditions. Propellant characterization can also be relatively slow due to the data analysis time required to ensure that samples did not contain voids or other defects. Using 2-D Digital Image Correlation (DIC) technology, a baseline behavior can be established for propellant samples that contain voids to help screen data faster, leading to a faster characterization time for propellants and reduced cost of the program. Overall, the DIC system is a promising method of non-contact strain measurement that can help characterize and screen solid composite propellants, while micro-dogbones show great promise in being able to reduce the time and cost required for characterizing novel solid propellants.

1. INTRODUCTION AND OVERVIEW OF MECHANICAL PROPERTY TESTING TECHNIQUES

1.1 Introduction and Solid Composite Propellants Overview

Solid propellants are used widely in the aerospace and defense fields owing to their diverse spread of applications, mechanical simplicity due to fewer components in the system, storability characteristics, and reliability. Early solid propellants, such as black powder, date back as far as the first millennium AD, where they were used for fireworks or gunpowder in China [1]. Today, solid composite propellants serve a wide variety of civil and military uses, from missiles and launch boosters to abort systems and hobby rockets. These propellants generally offer improved handling characteristics over their liquid counterparts. Additionally, solids offer a much higher thrust-to-weight ratio over liquid systems, volume specific impulse, and simplicity. Solid propellants are also often subjected to extreme conditions, such as rapid ignitions, thermal cycling outside the range of -50 ^{o}C to 50 ^{o}C, and high acceleration maneuvers. Research efforts have continued to characterize new propellants for improved systems and require new methods to develop these new propellants faster and at a reduced cost.

A solid composite propellant consists of several components, namely a solid particle oxidizer (typically about 200 μm in size) and possible metal fuel additive (typically aluminum about 15 μm in size), a polymer binder, a plasticizer agent to aid in the mixing process, a bonding agent to help strengthen the bonds between the polymer and solid particles, and a curative to help solidify the mixture. The "binder" of a solid propellant generally refers to the polymer, plasticizer, bonding agent, and curative, and makes up approximately 10-15% of a propellant formulation. This binder forms a mesh-like matrix around the solid particles to hold them in place. This is represented in Figure 1-1 [2].

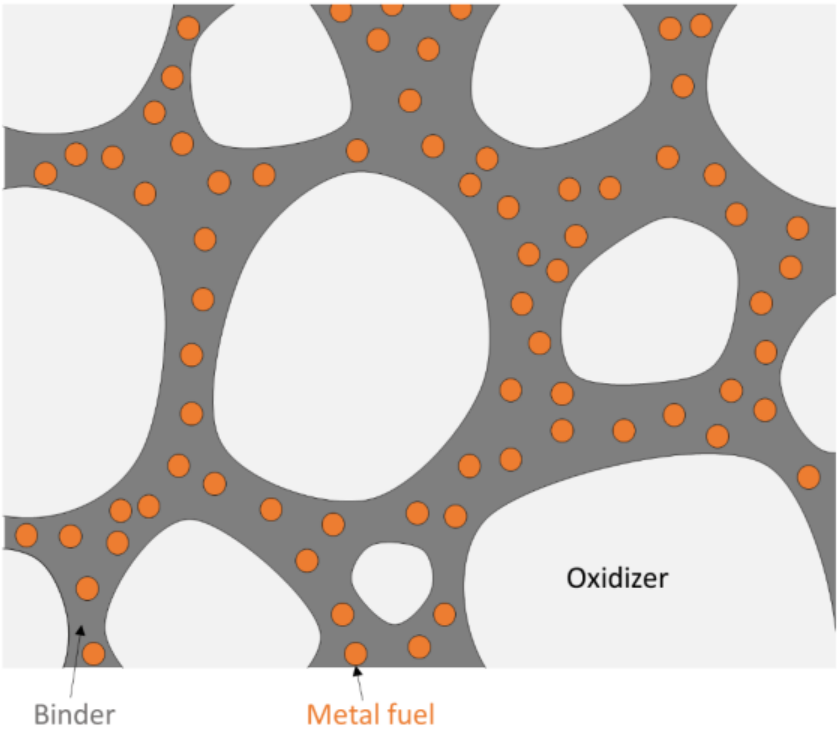

Figure 1-1. Representative Closeup Image of Solid Composite Propellant Makeup [2].

Today, most solid composite propellants tend to use ammonium perchlorate as the solid oxidizer, with aluminum being a common fuel additive [3]. A prepolymer is used to help hold these solid materials in place. These prepolymers are visualized as long molecular chains, akin to wet spaghetti noodles, which help form the matrix to hold the solid components. An ideal prepolymer will maximize the solids loading capability of the propellant, extend the storage life, and improve the mechanical properties across a wide range of operating temperatures [4]. Polybutadiene acrylonitrile, or PBAN, was the common selection for most propellants but has largely been replaced by Hydroxyl-Terminated Polybutadiene (HTPB). HTPB is preferred over PBAN for its excellent hydrolytic stability, compatibility with oil-type plasticizers, improved adhesions to substrates, and improved low-temperature properties [5]. Figure 1-2 displays the chemical structure of HTPB, illustrating the long chain of molecules that are the backbones of solid propellants [4].

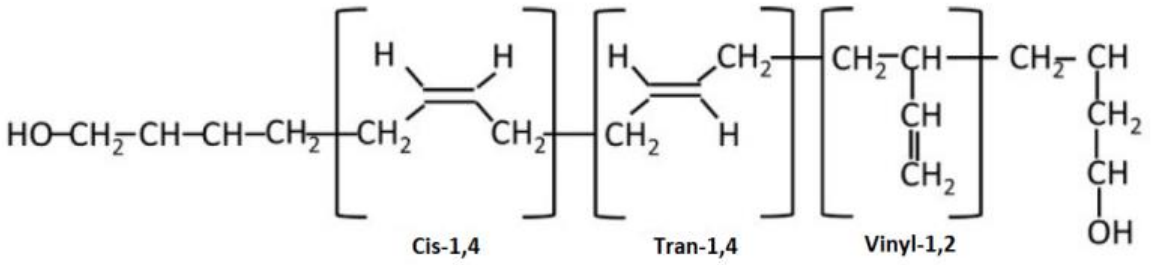

Figure 1-2. Chemical Structure of HTPB [4].

Ammonium perchlorate (AP) is the most widely used oxidizer in solid propellants due to its desirable compatibility, performance, and safety characteristics [3]. In solid propellants, AP (chemical structure: NH_4ClO_4) is usually in a blend of sizes from approximately 20-200 µm. Ammonium nitrate and potassium perchlorate have been occasionally used as oxidizers as well, but AP is the oxidizer of choice for most high-performance solid propellant applications.

For fuels, aluminum is the preferred choice, owing to its ability to increase combustion temperature, propellant density, and specific impulse, while being cheaper and more stable than most metals. A drawback of aluminum use in solid propellants is the formation of aluminum oxide in the combustion products, which is initially in the liquid phase, but condenses to a solid as the temperature drops in the exhaust gas and can produce slag in the motor nozzle, further decreasing performance by adversely affecting the mass ratio of the motor [3]. Boron is another fuel that has been explored but has not been implemented on a production scale due to the difficulties in achieving peak efficiency in burning at realistic chamber lengths. Beryllium also burns more easily than boron and has a higher volume specific performance, but is highly toxic to humans, and thus has not been used widely beyond research applications [3].

The plasticizers used in solid propellants help improve elongation properties, as well as processing capabilities, such as lower viscosity for casting [3]. Bonding agents can be used to help prevent “dewetting,” or the phenomenon of the solid particles separating from the binder matrix. As the solid particle separates from the binder around it, it weakens the propellant, leading to an early failure of the material [6,7].

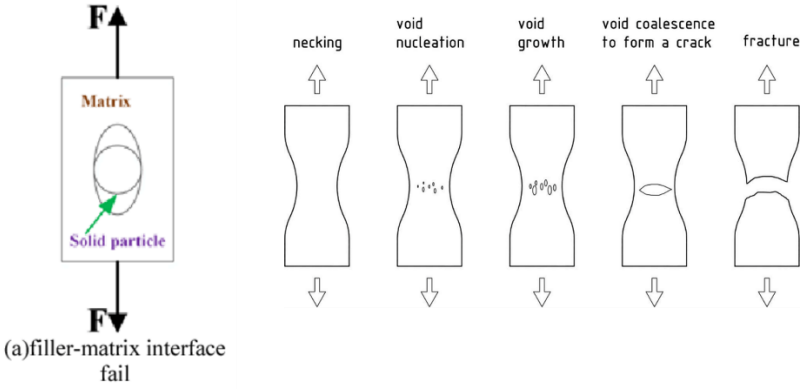

Figure 1-3. Visual Depiction of Void Formation Leading to Failure of the Material [6].

In curing agents, the isocyanate in the curative helps the long strands of binder attach to form the matrix in which the solid materials are held. Figure 1-4 illustrates the process of crosslinking, or how the isocyanate in the curative links the polymer strands together [8]. In this instance, HTPB is the polymer chain and isophorone diisocyanate (IPDI) is the curative. The isocyanate group (the -NCO group) is seen on the end of the carbon ring. This bonds with the hydroxyl (-OH) group on the HTPB to attach different strands of the polymer.

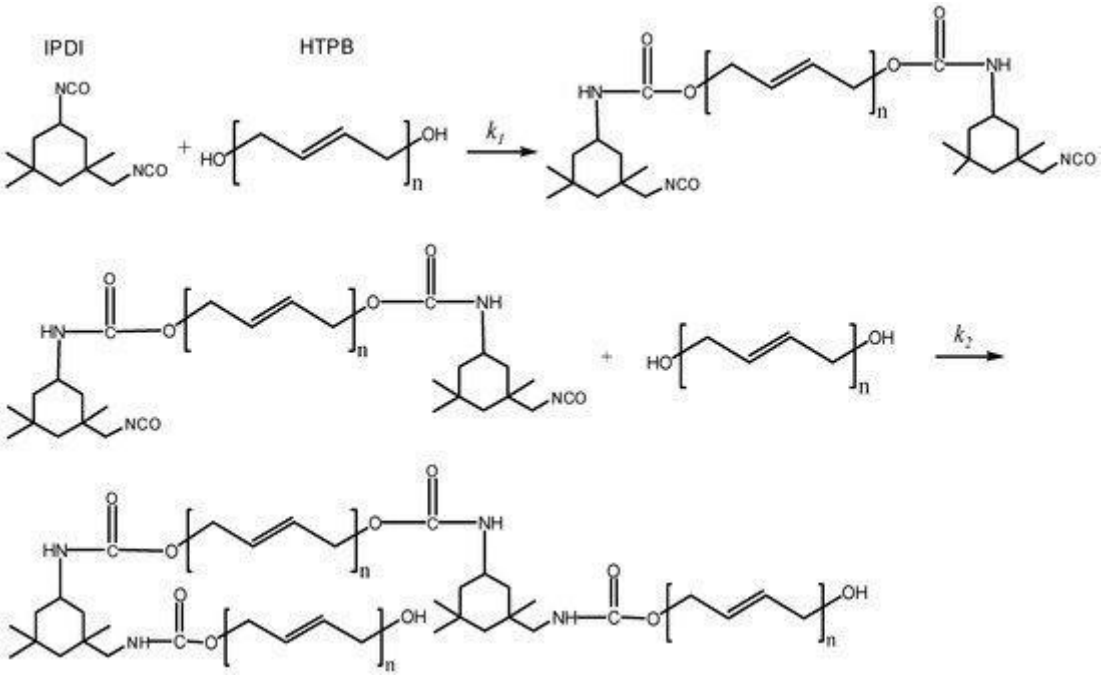

Figure 1-4. Visual Representation of Crosslinking for the HTPB and IPDI System [8].

In solid propellant formulations, the *isocyanate ratio* is the ratio of the number of isocyanate groups to the number of hydroxyl groups in a propellant. A ratio above unity results in a stiffer propellant, while lower ratios result in a softer propellant. Additionally, isocyanate groups can react with each other, forming dimers or trimers. Excess isocyanates that do not react with the hydroxyl groups in the HTPB will react with each other to form hard blocks in the matrix.

Overall, these solid propellant components are used together to create reliable, relatively safe, and high-performance flight systems for a wide range of military and civilian applications.

1.2 Uniaxial Tensile Testing

In Uniaxial Tensile Testing, a specimen is supported between two grips and pulled at a constant strain rate, while a load cell measures the force applied to the sample. By measuring the force, the stress experienced by the sample can be computed using Equation 1.

$$\sigma = \frac{F}{A} \quad \text{(Eq. 1)}$$

where σ is the normal stress at the cross-section of the dogbone being examined, F is the measured load, and A is the measured cross-sectional area of the gauge section sample or the middle portion between the grips. Figure 1-5 illustrates a propellant sample in the types of grips used for uniaxial tensile testing [9].

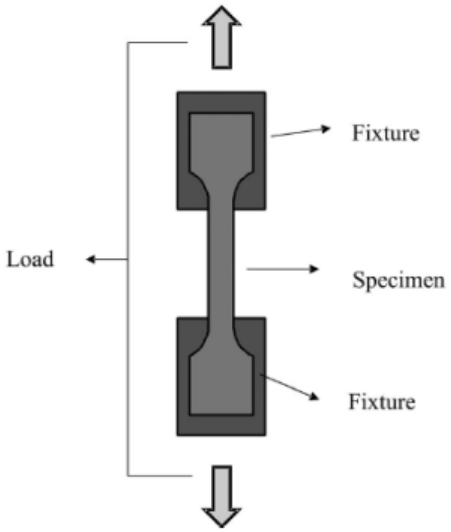

Figure 1-5. Representative Image of the Uniaxial Tensile Test Grips with Propellant Sample [9].

Strain, a property relating the deformation of a material to the stress exerted on it, is measured using Equation 2.

$$\varepsilon = \frac{\Delta L}{L_0} \times 100 \tag{2}$$

Here, ε is the strain (measured in percent), ΔL is the change in length of the sample, and L_0 is the original length of the sample. The final property of interest is the modulus of the material, which is a measure of stiffness. The modulus is found in the elastic region of the stress-strain curve (the linear portion before the yield strength marker), seen in Figure 1-6, and can be described by Equation 3 [10]. It is the change in stress in the linear elastic region, divided by the change in strain over the same region. It is worth noting that the solid composite propellants studied in this work are not linear elastic materials, but this model can be used for determining the modulus of the material. A higher modulus denotes a stiffer propellant, while a lower modulus signifies a more ductile one.

$$E = \frac{\Delta \sigma}{\Delta \varepsilon} \tag{3}$$

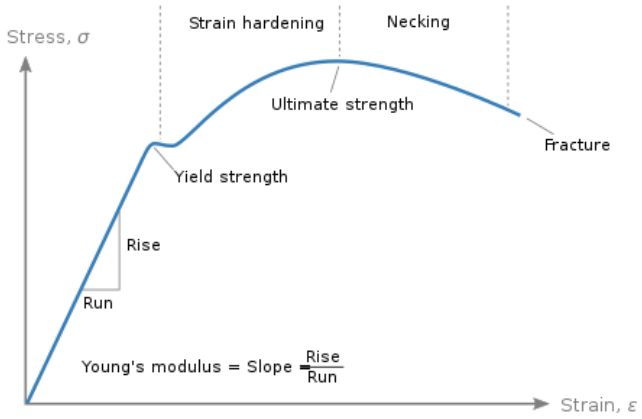

Figure 1-6. Stress-Strain Diagram With Various Mechanical Properties Depicted [10].

Historically, JANNAF Type C (Figure 1-7, left) samples in tensile testing have been used to study the mechanical properties of solid propellants. New research, however, has focused on testing "micro-dogbones" (Figure 1-7, right) [11-13]. Testing at smaller scales presents several advantages, including higher possible strain rates and the lower cost associated with producing less propellant.

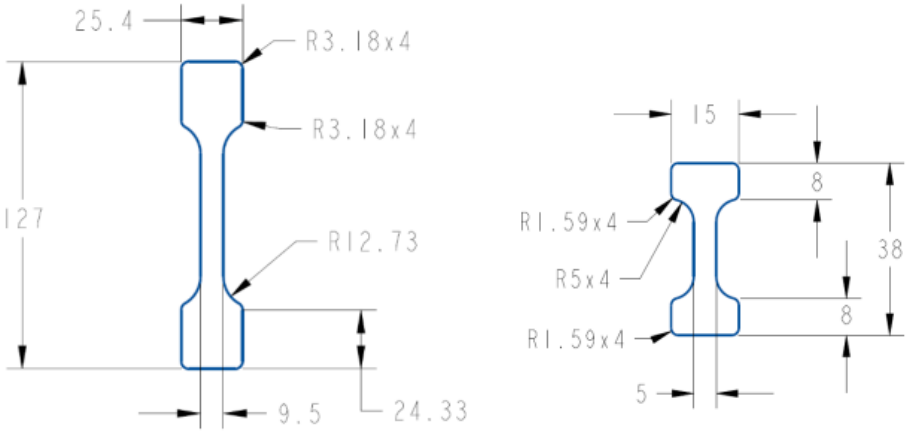

Figure 1-7. JANNAF (12.7 mm thick, left) and Micro (5 mm, right) Dogbone Sample Dimensions with units in millimeters.

Overall, Uniaxial Tensile Testing is a useful and widespread method for evaluating the mechanical properties of materials. It offers a simple, repeatable method for evaluating the

mechanical properties of materials that can output useful data about the solid propellant being evaluated.

1.3 Digital Image Correlation Overview and Background

Digital image correlation (DIC) refers to a non-contact strain measurement method that has gained popularity in recent years as the technology has become more refined. By applying a speckle pattern to a sample, the DIC system optically tracks the pattern and calculates localized strain because of this deformation and the change in position of each speckle. Figure 1-8 displays the general setup of the DIC system [9].

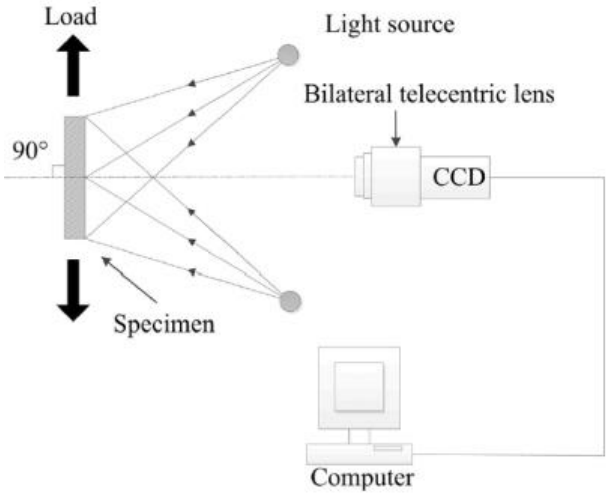

Figure 1-8. Digital Image Correlation System Set Up.

The software used can then interpret the speckles' displacement over time to generate a strain field, as seen in Figure 1-9. The speckles' displacement using a known distance, such as a predetermined distance between two lines, as can be seen in Figure 1-9. To calibrate the length, a digital gauge is placed on the top part of the upper black line, while another is placed on the bottom of the lower line. A digital extensometer is then created from these two lines, with the number of pixels between the two gauges correlating to the length. For the JANNAF dogbones, the 40 mm length used equated to 435.56 pixels, while the micro-dogbones used a gauge length of 10 mm, or 317.03 pixels. A possible source of error could come from being off in the placement of the digital

gauges, as being 1 pixel off would result in a 0.229% and 0.315% error for JANNAF and micro-dogbones, respectively.

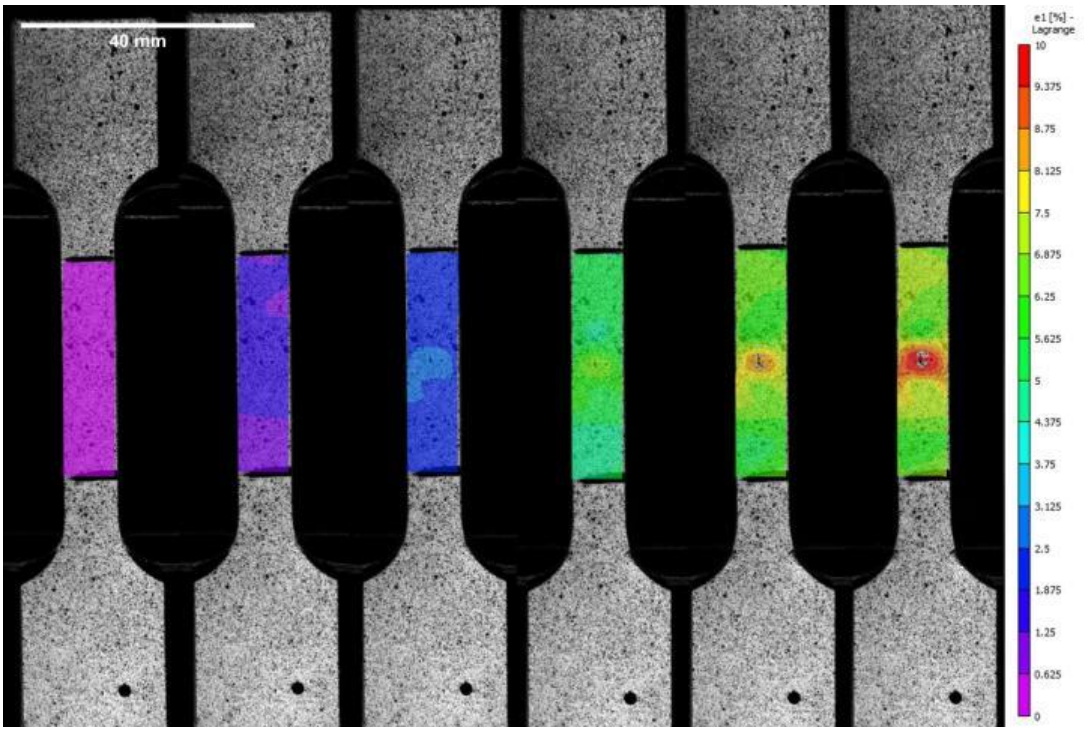

Figure 1-9. Representative Image of Strain Field Superimposed on JANNAF Dogbone by DIC Software during Uniaxial Tensile Testing.

As seen above, the DIC displays the gauge section of the speckled dogbone and the heatmap corresponds to areas of high strain before, ultimately, the sample fractures. In Figure 1-9, areas of purple and blue relate to areas of low strain, while orange and red signify higher strain concentrations. As expected, the strain is typically observed to be highest where the sample eventually breaks.

Having a non-contact method of evaluating strain is useful for the micro-dogbones as the effects of attaching a physical extensometer could prevent accurate data collection. This is an improvement over laser extensometers as well since by generating a strain field as opposed to a single global strain measurement, anomalous behavior such as voids or fractures can be detected faster, allowing for more precise data analysis. This is significant since it allows for an outlier containing a void to be determined from a single test, rather than needing to examine multiple test samples to detect an outlier.

1.4 Research Objectives

In this work, the main research objective is to characterize solid propellants at both JANNAF and micro-dogbone scales to examine the correlation between the sample sizes for their mechanical properties (namely the ultimate stress on the propellant, the strain at ultimate stress, and the modulus of the propellant). This is done to evaluate the merits of the smaller sample size to see if these micro-dogbones can replace the industry-standard JANNAF samples and reduce the time and cost required to formulate and study new solid composite propellants.

Another goal of this work is validating 2-D Digital Image Correlation as a useful tool for non-contact strain measurement for solid propellant sytems, as well as a method of screening out anomalous samples. Part of this work will involve placing glass beads of varying sizes in dogbone samples to test the capabilities of the DIC system in finding these manufactured voids. Examining the changes in mechanical properties because of the glass bead insertion will help model the effects of voids or other defects that can be found in propellants. These results will establish a baseline for samples containing voids, which will help prevent poor data collection for other experiments.

The propellants will then be examined across a wide range of formulation changes to accurately capture the changes in mechanical properties between sample sizes. Various formulation parameters will be changed, including plasticizer and bonding agent content, isocyanate ratio, solids loading, and the size of AP used.

The final portion of the research is to examine the effects of temperature on the mechanical properties of the solid propellants, and how well the micro-dogbones correlate to the JANNAF size at low temperatures. By testing at -60 ^{o}C, -30 ^{o}C, 0 ^{o}C, 25 ^{o}C, and 60 ^{o}C, the material response across a wide range of temperatures can be examined, leading to a more thorough understanding of the effects of sample size in relation to the temperature changes.

In the following chapters, this thesis will lay out a detailed summary of the history of mechanical property empirical and theoretical work relating to solid composite propellants. This work aims to help improve the process, length of time, and cost required to mechanically characterize solid composite propellants, as well as gain a more complete understanding of the effects of sample size on key mechanical properties.

2. LITERATURE REVIEW

2.1 Previous Mechanical Properties Research on Solid Composite Propellants

Understanding the mechanical properties of solid propellants is important as each application may require different characteristics and metrics. A propellant's resistance to fracture is evaluated by its tensile strength and elongation capability. This is an important characteristic for rocket motors due to the forces experienced during high acceleration maneuvers often encountered during flight for these systems. Cracked propellant will lead to a failed motor, making it paramount that the propellants selected for these purposes have optimized mechanical properties.

Mechanical properties have been studied extensively for solid propellants, and the effects of temperature and strain rate have been well-documented. Adel et al. found that the strain of HTPB-based materials decreased with increasing temperature as the high temperature (+80 ^{o}C) caused the crosslinking chains in the polymer to fail earlier in the stress-strain curve, thus reducing the modulus and maximum stress as well [14]. This is illustrated in Figure 2-1, where for constant crosshead speed during uniaxial testing, the modulus, maximum stress, and strain capability decrease with increasing temperature.

Within solid propellant investigations, Bose and Pandey examined the role that bond strength plays in the mechanical properties of solid propellants and determined that bond strength of the solid particles to the surrounding binder is a more important factor than ultimate strength in preventing the failure of the propellant grain [15]. Chain extenders have also been used to examine if the ultimate strength can be increased without sacrificing elongation characteristics, to some degree of success [16].

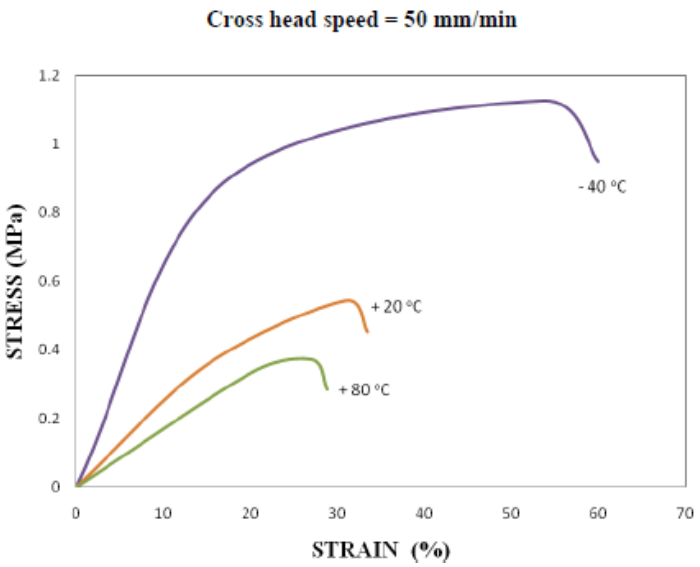

Figure 2-1. Mechanical Properties of HTPB-based Materials Decreasing with Increasing Temperature for Constant Crosshead Speed During Uniaxial Tensile Tests [14].

In addition to temperature effects, the mechanical properties of solid propellants are also affected by the internal bonding forces of the solid particles to the binder matrix. Examining the causes of dewetting, Oberth displayed how the stresses around a solid particle in a binder matrix are strongest at the poles, as seen in Figure 2-2 for loading in the vertical direction[17].

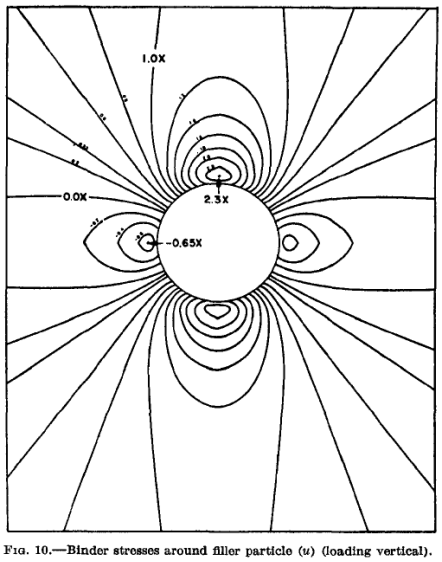

FIG. 10.—Binder stresses around filler particle (u) (loading vertical).

Figure 2-2. Strain Field Around a Solid Particle in a Polymer Matrix [17].

Similarly, Gent and Park examined the stresses around solid particles in filled rubbers and found that the cohesive debonding process begins with cavitation, where a small cavity forms in the matrix near, but not on, a solid particle [18]. Additionally, this work found that the cavitation and debonding stresses are dependent on the Young's Modulus of the material, where cavitation occurs with microvacuoles appearing in the material at a stress equal to 5/12 of the Young's Modulus for larger particles. For adhesive debonding, however, it was found that the stress required for debonding decreased with increasing modulus, and the debonding stress was tied to particle size, proportional to $d^{-1/2}$, where d is the diameter of the particle [18]. Toulemonde et al. examined similar effects with highly filled elastomers and displayed that a mix of both large and small particles helped prevent the formation of early cracks that lead to failure [19]. Ashish et al. also found that a higher ratio of coarse and fine AP particles in a solid propellant helped increase the tensile strength and modulus of the propellant due to the improved volume packing, where the bonding agent has more surface area to bond to because of the addition of the fine particles [20].

To try and combat the effects of debonding, a great deal of research has examined bonding agents and the various roles they play in improving mechanical properties. As expected, research in this area has shown that the presence of bonding agents increases the maximum stress and strain at the ultimate stress of a propellant, thus improving the overall mechanical properties [21]. These improvements help with preventing debonding during various stresses, even low-magnitude ones encountered during storage [22]. Several types of bonding agents have been studied, and Yadav et al. demonstrated how amine-based bonding agents, such as Tepanol, are adsorbed directly onto the surface of the AP particle in the binder matrix, forming a tough shell around this particle [23]. In aziridine-based bonding agents, such as 1,1-Isophthaloyl bis 2-methylaziridine, otherwise known as HX-752, the bonding agent is soluble in the HTPB binder and bonds the particle directly to the matrix by adhering to the solid AP particles and forming a tough shell around them, which is then crosslinked into the polymer matrix [23]. A small drawback of these bonding agents is ammonia gas produced during the bonding process, which adds safety considerations to the mixing process and increased potential for void formation during curing as ammonia bubbles could be trapped in the propellant composition. Additionally, isocyanate would then react with the ammonia instead of the polymer chains, leading to a much softer propellant than designed. This can be

prevented by allowing the mixture to off-gas over a longer period of time, such as overnight), before the curative is added and final casting occurs. Aziridine bonding agents, however, produce orders of magnitude less ammonia than amine bonding agents, which is an attractive quality to consider in the propellant formulation process. Overall, bonding agents play a key role in helping improve the mechanical properties of solid propellants.

2.2 Small-scale Testing of Solid Propellant Mechanical Properties

The ability to reduce the testing to small-scale experiments would allow new propellants to be characterized faster and at a lower material and labor cost than current industry methods. Overall, there have been minimal studies done on small sample sizes, but some data suggest that data differs between large and small tensile specimens, although that was attributed to inhomogeneity [21]. Benedetto, van Ramshorst, et al. looked at quarter-size JANNAF dogbones using a scanning electron microscope (SEM) and found that inhomogeneities present in the propellant composition would have a greater effect at the small scale [12,13]. Siviour, et al. found that the larger relative size a particle has to the matrix cross-sectional area the more the overall strength decreases [24]. This research has helped refine the efforts to measure the mechanical properties of propellants at smaller scales than typically seen in laboratory settings, such as JANNAF Type C-sized samples. Testing at smaller scales presents several advantages, including higher possible strain rates and the lower cost associated with producing less propellant [25].

2.3 Research using Digital Image Correlation for Solid Propellant Research

During uniaxial tensile testing, materials that experience a large strain may have an overestimate of the true stress due to constant volume assumptions, but the volume of the test article will change at high strain values. G'Sell et al. and Monhanraj addressed this by optically tracking dots applied to the surface of test samples to calculate the axial strain based on the displacement of these markings [26, 27]. Ranjan et al. used this technique to demonstrate the differences between nominal strain computed by a uniaxial tensile test and the true strain measured by a DIC system for the same sample [28].

Digital Image Correlation also offers the advantage of being able to screen out test samples containing voids prior to data analysis, which would help with improving data collection, while reducing the time and cost associated with regular data analysis processes. Miller, et al. found consistent measurements between their DIC system and a laser extensometer that measured the same sample and were able to calculate Poisson's Ratio for both solid composite and double base propellant samples, helping demonstrate the capabilities of a DIC system in propellant characterization [29]. Cui et al. also used DIC to measure the Poisson's ratio and Young's Modulus in solid propellants and were able to successfully characterize a propellant over the temperature range of -30 ^{o}C to 70 ^{o}C for use in a time-temperature superposition analysis [9]. Zhu et al. successfully used DIC techniques to quickly determine the elastic constants and tensile strength of energetic materials to optically measure in-plane displacement fields [30].

Digital Image Correlation remains, however, a relatively unused tool for solid composite propellant testing, as most test methods prefer laser or physical extensometers, and has not been used as a method for screening out anomalous samples.

3. EXPERIMENTAL METHODS AND TEST PHASES

3.1 Sample Preparation

In this work, a baseline propellant was made (as listed in Table 3-1): 85%wt. solids loading including ammonium perchlorate as the solid oxidizer (AP, 200:20 μm coarse particle blend with 70:30 coarse to fine ratio, from RCS Rocket Motor Components) and 15-μm aluminum metal fuel additive (from Valimet). The binder (15%wt.) was comprised of hydroxyl-terminated polybutadiene (HTPB HTLO, RCS), isodecyl pelargonate (IDP, RCS) plasticizer, triphenyl bismuth cure catalyst to reduce cure time, HX-752 (from 3M) as the bonding agent, and isophorone diisocyanate (IPDI, RCS) as the curing agent, all with an isocyanate ratio of 0.9. The baseline formulation was then varied as shown in Table 3-2. Dimensions for the JANNAF Type C and micro-dogbones were shown previously in Figure 1-6, with JANNAF dogbones having a gauge length of 40 mm and the micro-dogbones having a gauge length of 10 mm.

Table 3-1. Baseline Propellant Formulation Used in This Study.

Ingredient Type	Ingredient Name	wt%
Binder		
Polymer	HTPB HTLO	10.73
Plasticizer	IDP	3
Bonding Agent	HX-752	0.25
Cure Catalyst	Triphenyl Bismuth	0.02
Curing Agent	IPDI	1
Solids		
Oxidizer	Ammonium Perchlorate	67
Metal Additive	Aluminum	18

Table 3-2. Formulation Changes from Baseline.

Formulation Iteration	Change from Baseline
1	Increased Plasticizer Content to 6% by wt
2	Decreased Plasticizer Content to 2% by wt
3	Increased Bonding Agent Content to 0.5% by wt
4	Decreased Bonding Agent Content to 0% by wt
5	Decreased Curative Ratio to 0.75
6	Increased Particle Size blend to 400 µm AP
7	Increased Solids Loading to 87%
8	Decreased Solids Loading to 83%

The propellants were mixed using a 1-qt Ross Dual Planetary Mixer at 50 °C water jacket temperature while drawing a vacuum. They were poured into tray molds and cured at 60 °C for 5 days. After curing, samples were created using custom-ordered cutters from Kind Snail Ltd. A diagram of the Ross Mixer is shown in Figure 3-1, while the Kind Snail cutters are depicted in Figure 3-2 [31]. Samples were chosen to be cut, rather than cast to shape or milled, owing to the simplicity of mold design using this method, and the difficulty involved in extracting the micro-dogbones from a small cast mold.

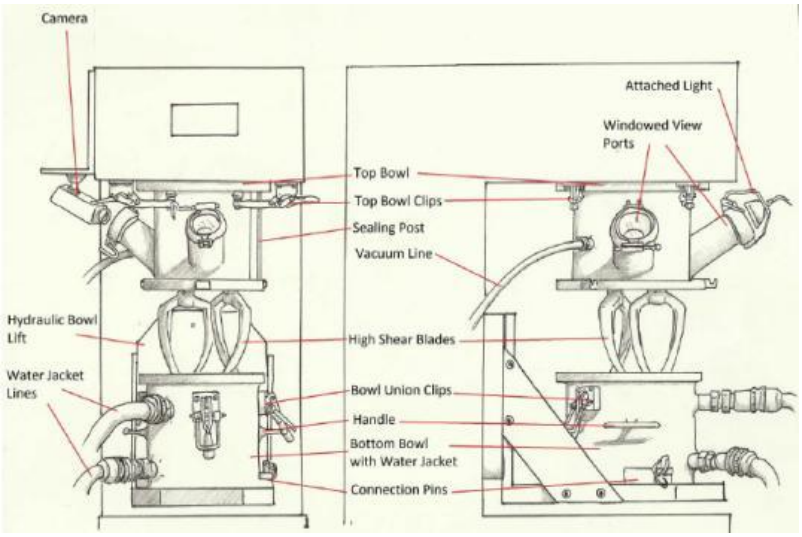

Figure 3-1. Ross Mixer Diagram [31].

Figure 3-2. Kind Snail Cutting Dies.

3.2 Test Methods

Samples were spray-painted white and speckled with black spray paint for use with the DIC system. An ADMET 2600 tensile tester was with a 300-lbf load cell and in-house built fixed grips, and a 2-D DIC system (VIC-2D) is from Correlated Solutions, Inc. Tests were performed at 25 °C and strain rates for the propellant changes were held constant at 0.0021 s^{-1} (5 mm/s crosshead speed for JANNAF C dogbones) for consistent behavior between the JANNAF and micro samples. In the experiments examining temperature changes, strain rates were increased to 0.021 s^{-1} (50 mm/s crosshead speed for JANNAF C dogbones) to match previous literature data for direct comparison of test methods and results. A basic overview of the tensile tester and DIC system is shown below in Figure 3-3, with the real system seen in Figure 3-4. Stress was measured by the load cell on the uniaxial tensile tester, while strain data was collected by the DIC system. Young's Modulus was calculated from the MTest Quattro Software on the control computer that controls the tensile, using a secant method that involved finding the stress at 0.3% and 2% strain and using the previously mentioned Equation 3 to calculate modulus. Samples are pushed to the back of the grips (as seen in Figure 3-5), allowing them to fully interface and avoid shear stress from affecting the results.

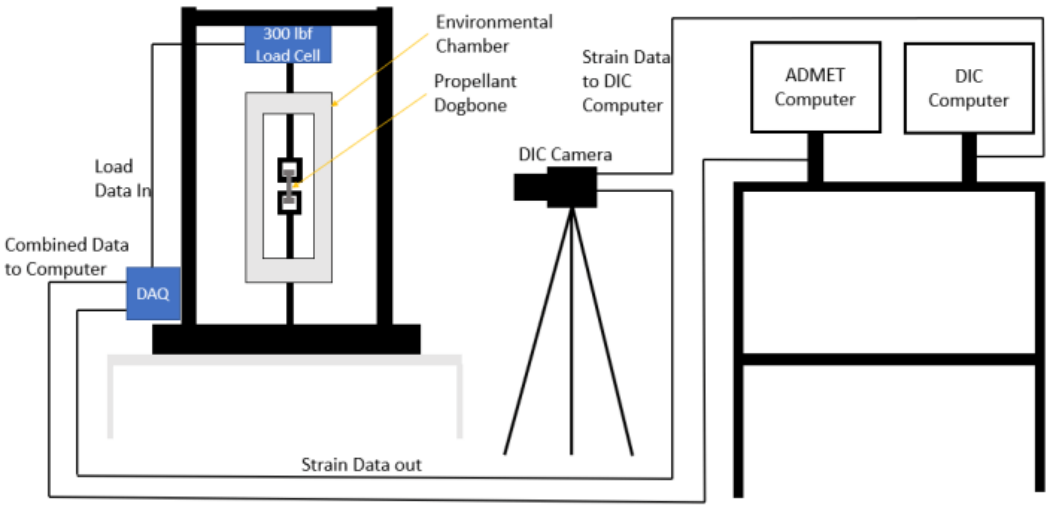

Figure 3-3. Basic Schematic Showing the Test Setup for the Tensile Tester and DIC Systems.

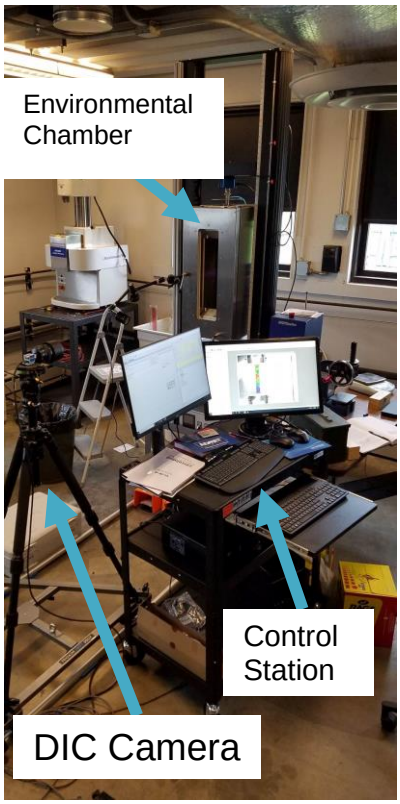

Figure 3-4. Experimental Setup Used for Mechanical Property Testing.

Figure 3-5. Fixed Grips Designed for Tensile Tests with JANNAF (Left) and Micro (Right) Sizes.

Part of this investigation will be to test the capabilities of the DIC system by using samples with manufactured voids (in this case glass beads) and observing how quickly the DIC system can identify these voids. In doing this, the DIC system can be shown to be a superior alternative to traditional extensometers. For the void investigation, four different sizes of uncoated polished soda lime glass beads (2500, 1000, 500, and 200 μm diameter) were placed in the dogbone during the mixing process to create a manufactured void in the approximate middle of the dogbone. The glass beads were chosen due to the binder having a low adhesion to the glass surface, allowing for the simulated void effect. Five JANNAF and five micro dogbones were run for each bead size, resulting in a test matrix of 40 dogbones. These samples were tested at the same conditions as above, and the DIC was used to establish failure criteria for samples based on the response of the

sample to the manufactured void. The beads were procured from Cospheric LLC and added to the samples at the end of the mix cycle and can be seen below in Figure 3-5.

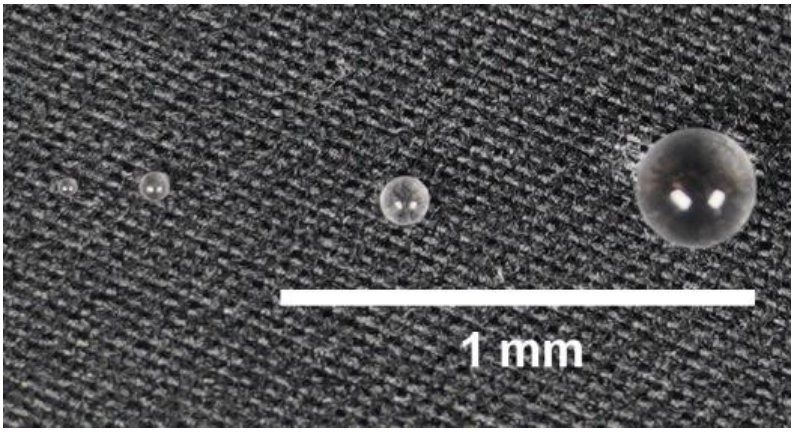

Figure 3-6. From Left to Right: 200 µm, 500 µm, 1000 µm and 2500 µm Glass Beads That Were Placed in the Dogbones.

To perform the environmental testing, liquid nitrogen was used to chill the chamber by attaching a dewar to the back of the environmental chamber and setting the desired temperature of the test on the tensile tester's interface panel. Heating the chamber involved setting the raised temperature on the interface panel and allowing the environmental chamber to raise the temperature through electrical heating. Samples sat inside the chamber for 1 hour before testing to ensure that the sample itself was at the same temperature as its surroundings. Tests were performed at -60 ^{o}C, -30 ^{o}C, 0 ^{o}C, and +60 ^{o}C, along with the +25 ^{o}C (room temperature) tests previously performed, to get a broad understanding of the material properties across a wide temperature range.

3.3 Test Matrices

Initially, the test matrix was as seen below in Table 3-3. A minimum of three dogbones were tested at each sample size for each test from each batch. This allowed for increased confidence in data collection and trend analysis while balancing the time and schedule demands of the project and reducing possible error from inter-batch variation.

Table 3-3. Phase 1 Test Matrix for Propellant Study.

Mechanical Properties Test Matrix	Objective	Formulation	Notes
Baseline Mix	Create baseline mix to use for propellant study	DF.007.DP.PO.04.001	Baseline Mix
Void Investigation, Large Beads	2500 µm Beads in Samples	DF.007.DP.PO.04.015	Finish void investigation with 2500 µm beads
Void Investigation, Medium Beads	1000 µm Beads in Samples	DF.007.DP.PO.04.015	Finish void investigation with 1000 µm beads
Void Investigation, Small Beads	500 µm Beads in Samples	DF.007.DP.PO.04.014	Finish void investigation with 500 µm beads
Void Investigation, XS Beads	200 µm Beads in Samples	DF.007.DP.PO.04.016	Finish void investigation with 200 µm beads

Table 3-4. Phase II Test Matrix for Propellant Study.

Mechanical Properties Test Matrix	Objective	Formulation	Notes
Plasticizer Content Effects I	Observe the change in mechanical properties for increasing plasticizer content	DF.008.DP.PO.04.001	Doubles (6% wt.) the plasticizer content from the baseline configuration (3% wt.)
Plasticizer Content Effects II	Observe the change in mechanical properties for decreasing plasticizer content	DF.009.DP.PO.04.001	Reduces plasticizer content by 33% (2% wt.) from the baseline configuration (3% wt.)
Bonding Agent Effects I	Observe the effects of changing the amount of bonding agent from the baseline configuration	DF.010.DP.PO.04.001	Doubles (0.50% wt.) the Bonding Agent content from the baseline configuration (0.25% wt.)
Bonding Agent Effects II	Observe the effects of changing the amount of bonding agent from the baseline configuration	DF.011.DP.PO.04.002	Removes (0% wt.) the Bonding Agent content from the baseline configuration (0.25% wt.)
Isocyanate Ratio	Varies the Isocyanate Ratio	DF.012.DP.PO.04.001	Reduces Isocyanate Ratio to 0.75 to compare to previous 0.9 ratio mixes
Solids Loading I	Vary Solids Loading % from 85% to 87%	DF.013.DP.PO.04.001	Increases Solid Loading by 2% from the baseline configuration
Solids Loading II	Vary Solids Loading % from 85% to 83%	DF.014.DP.PO.04.001	Decreases Solid Loading by 2% from the baseline configuration
Particle Size	Increase coarse AP from 200 µm blend to 400 µm micron blends and observe the effects	DF.015.DP.PO.04.001	Increased coarse AP size from baseline (baseline: 200 µm, new: 400 µm)

Table 3-5. Phase II Test Matrix for Propellant Study.

Mechanical Properties Test Matrix	Objective	Formulation	Notes
Low Temperature Effects Part 1	Decrease Environmental Chamber to -60 ºC	DF.007.DP.PO.04.008	Decrease temperature to compare to baseline
Low Temperature Effects Part 2	Decrease Environmental Chamber to 0 ºC	DF.007.DP.PO.04.009	Decrease temperature to compare to baseline
Low Temperature Effects Part 3	Decrease Environmental Chamber to -30 ºC	DF.007.DP.PO.04.011	Decrease temperature to compare to baseline
High Temperature Effects	Increase Environmental Chamber to 60 ºC	DF.007.DP.PO.04.006	Increase Temperature to compare to baseline

This series of tests was used to help maintain the scope and schedule of the overall project while providing ample changes to the baseline formulation and environmental conditions to properly examine the differences and correlations therein.

4. RESULTS AND DISCUSSION

4.1 Void Investigation Results

In the void investigation, the samples were analyzed to compare the global strain of the sample to the local area where the first signs of sample break were observed to occur to measure the difference between them. In this case, "global strain" refers to the strain experienced by the entire gauge section (the area from the top of the upper black line to the bottom of the lower black line) while "local strain" refers to a small area within the gauge section that is analyzed separately, and is measured as the area where the sample is observed to break. Figure 4-1 illustrates the difference between these two areas.

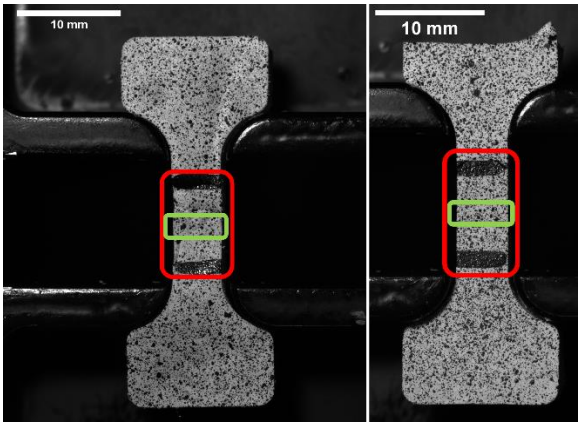

Figure 4-1. Baseline Dogbone (Left) and Dogbone with 2500 um Glass Bead (right), with Global (red) and Local (green) Strain Areas Highlighted.

On average, a void in the sample results in a significant change in global versus local strain behavior. From this analysis, it is then possible to visualize the strain field on the sample using the DIC system. In Figure 4-2, the technique is used to great effect to visualize the strain field on the sample, and it is easy to observe the formation and propagation of the voids as the sample breaks along where the bead is located. This is illustrated by Figure 4-3, where the baseline sample is analyzed alongside a sample containing a 2500 μm glass bead, and their global and local strain versus time graphs are compared. Table 4-1 compares the average percent difference in local versus global strain, as measured at peak strain values for each data set.

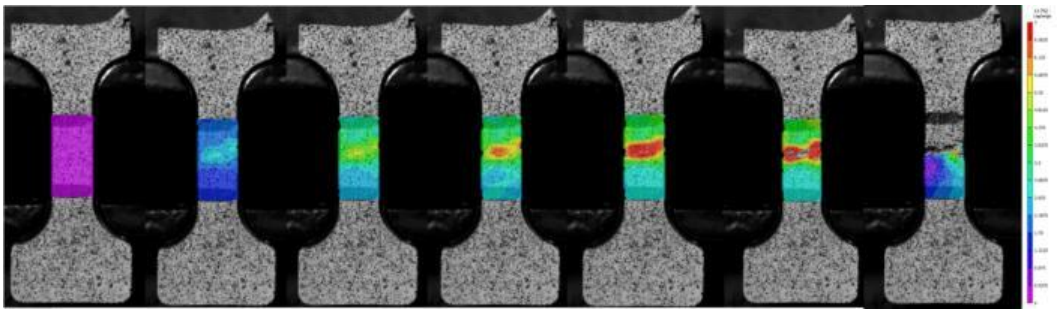

Figure 4-2. Representative DIC Image Sequence Showing Strain Field and Void Formation Leading to Fracture.

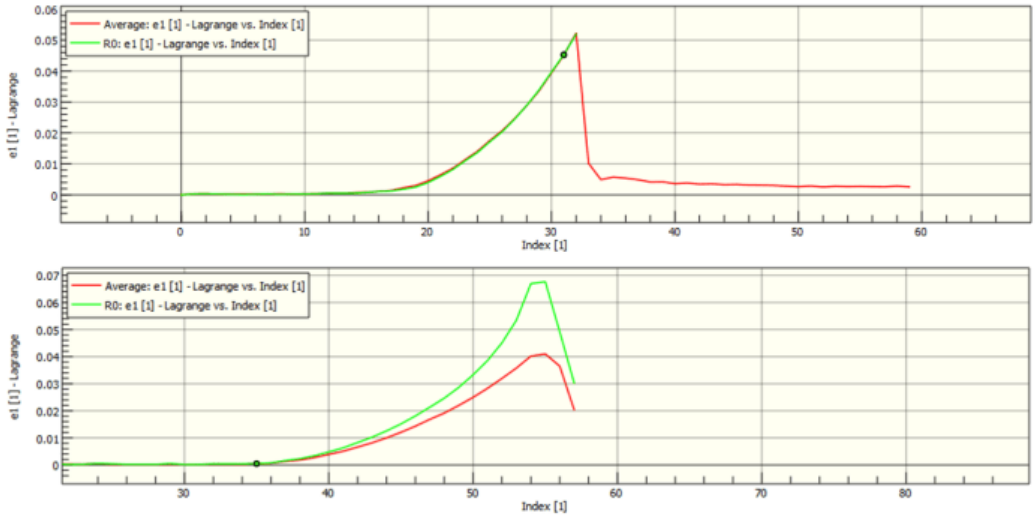

Figure 4-3. The Difference in Local (Green) vs. Global (Red) Strain Over Time in a Baseline JANNAF Sample (Top) and Manufactured Void Sample with 2500 µm glass bead (Bottom).

Table 4-1. Average Percent Difference in Global vs. Local Strain.

BEAD SIZE	Δ%, MICRO	Δ%, JANNAF
None	5.44	5.25
200 µm	25.26	1.19
500 µm	40.66	32.44
1000 µm	42.31	8.62
2500 µm	33.05	21.91
Any Bead	35.85	17.66

Figure 4-4 displays the same sample after testing, and it is confirmed by visual inspection that the sample broke where the bead is located at the back of the gauge section when facing the camera. Figure 4-5 shows a representative stress-strain graph that compares the behavior of the samples for different bead sizes. As seen in Figures 4-2 and 4-3, the DIC system is effective in capturing voids predictably and even captured the bead pictured in Figure 4-4, even though it was located on the far side of the sample. It is a good method for analyzing the strain fields of test articles and quickly identifying outliers. As seen in Figure 4-5, the larger the bead, the sooner the sample breaks. 2500 µm defects are unlikely, but Table 4-1 displays that the local vs. global strain disparity trend is visible even at the 500 µm threshold, a reasonable size for a potential void. This analysis would allow for an anomalous sample to be detected early in the testing process, as it can be seen how the samples break sooner with voids compared to the samples without manufactured voids.

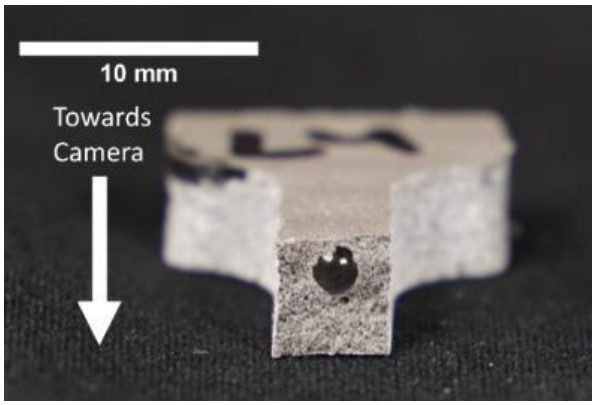

Figure 4-4. Representative Image of Sample with Glass Bead Embedded.

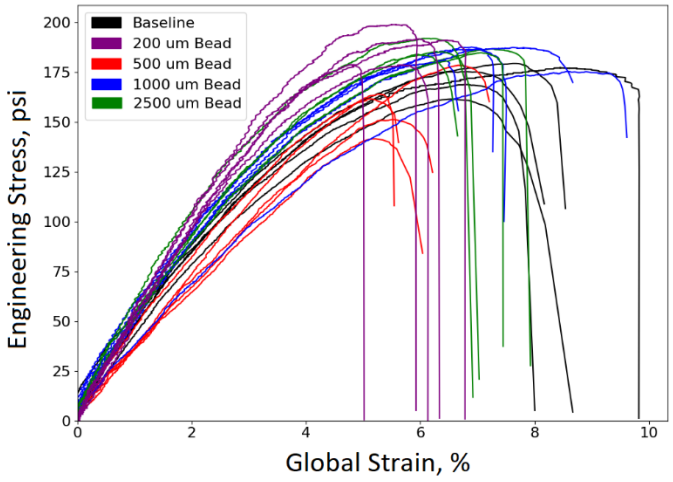

Figure 4-5. Representative Stress-Strain Diagram of JANNAF Samples with Different Bead Sizes.

4.2 Analysis of Mechanical Properties due to Formulation Change

The different batches introduced above were mixed, cured, prepared, and tested, resulting in the stress-strain data seen in

Table **4-2.** Figure 4-6, Figure 4-7, and Figure 4-8 represent the difference in mechanical properties between sample sizes for the baseline formulation, a batch displaying a strong correlation, and a batch that demonstrated a weaker correlation. The stronger correlation between the sample sizes was observed in the batch with an increased solids loading (87%wt.), while the lower correlation came from the batch with 400 µm AP blend in place of the baseline 200 µm AP

blend, which tracks with the expected behavior for the larger relative size of the solids compared to the binder matrix. Figure 4-9, Figure 4-10, and Figure 4-11 display the overall comparison of how the different sample sizes match up relative to one another. Within these plots, the error bars display the standard deviation for each sample size and formulation, although the limited sample size results in a lower statistical significance. They are useful, however, as a visual aid for correlating the sample sizes to each other. From these plots, and the tabulated results, it can be observed that the various changes made to the baseline propellant formulation resulted in noticeable changes in ultimate stress, strain at ultimate stress, and Young's Modulus. Additionally, Figure 4-12, Figure 4-13, and Figure 4-14 illustrate the relationship between average ultimate stress, average strain at ultimate stress, and average Young's Modulus for the two different sample sizes, confirming that there is a relationship between mechanical properties and sample size. A physics-based linear regression model (where the correlation is modeled as $y = ax$) was applied to calculate the R^2 value for each property.

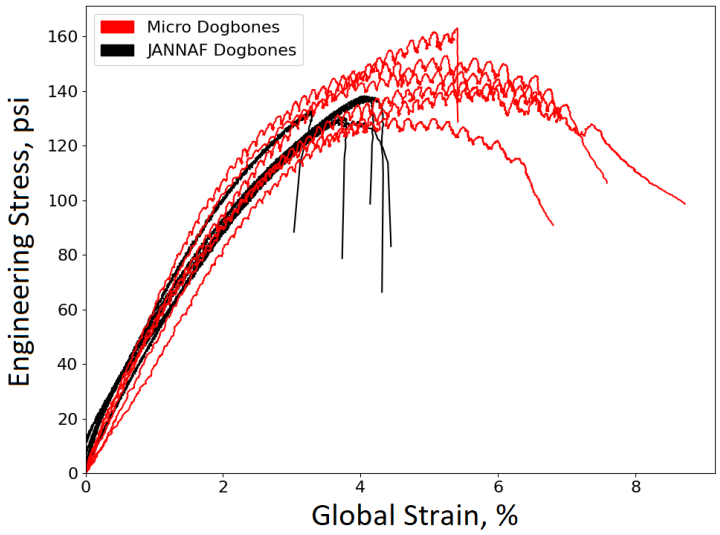

Figure 4-6. Stress-Strain Graph of JANNAF vs. Micro Samples for the Baseline Formulation.

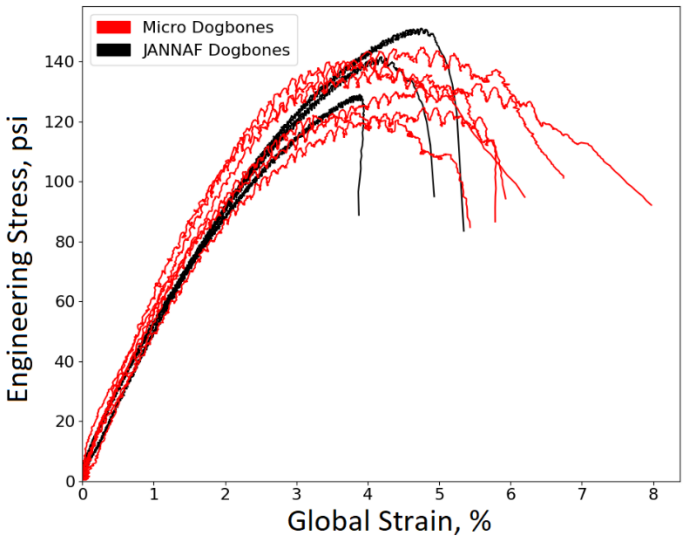

Figure 4-7. Representative Stress-Strain Graph of JANNAF vs. Micro Samples for Increased Solids Loading, Depicting A Strong Correlation.

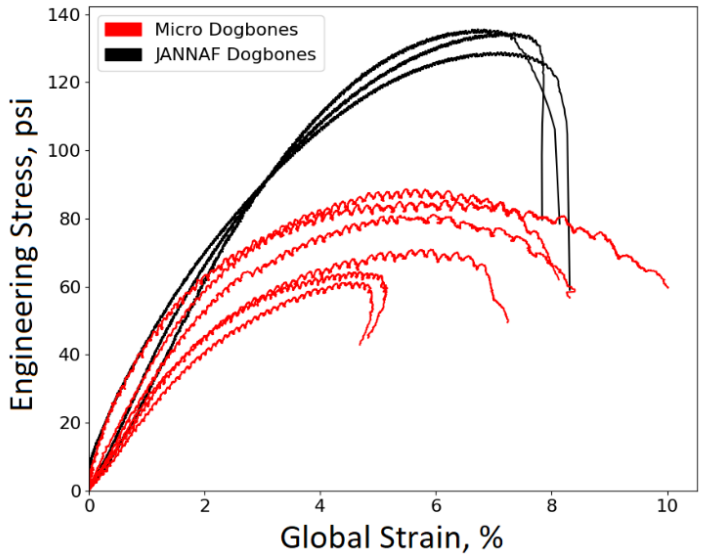

Figure 4-8. Representative Stress-Strain Graph of JANNAF vs. Micro Samples for Increased AP Particle Size, Depicting A Weaker Correlation.

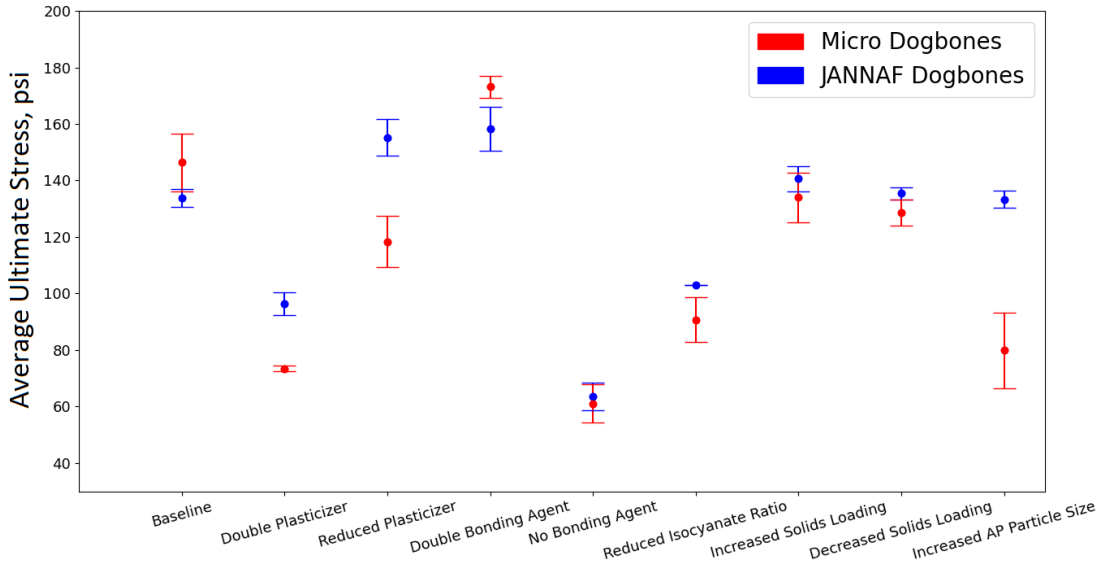

Figure 4-9. Distribution of Average Ultimate Stress Data Across All Formulations.

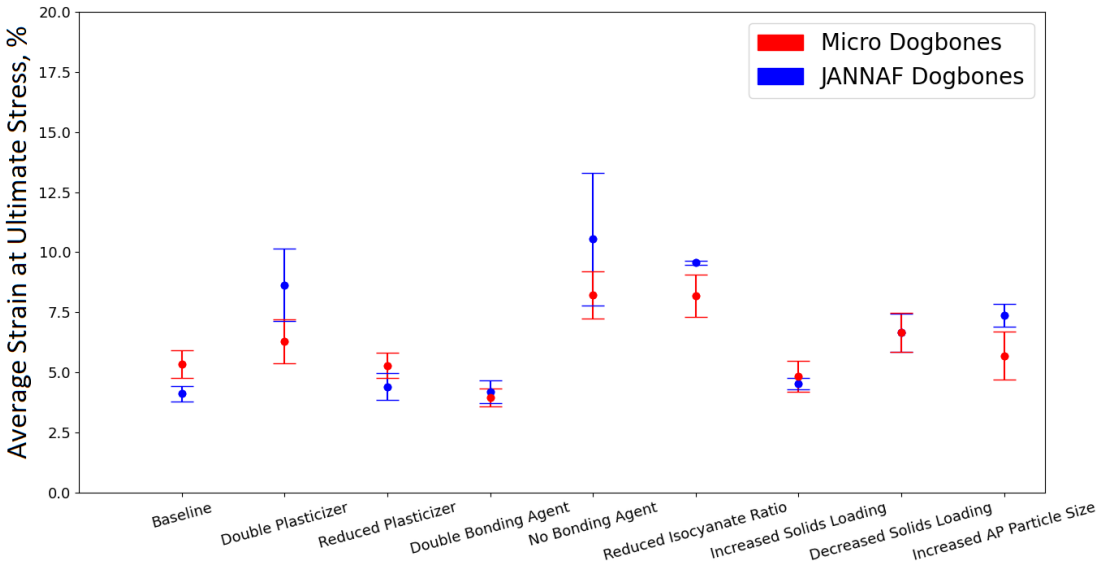

Figure 4-10. Distribution of Average Strain Data Across All Formulations.

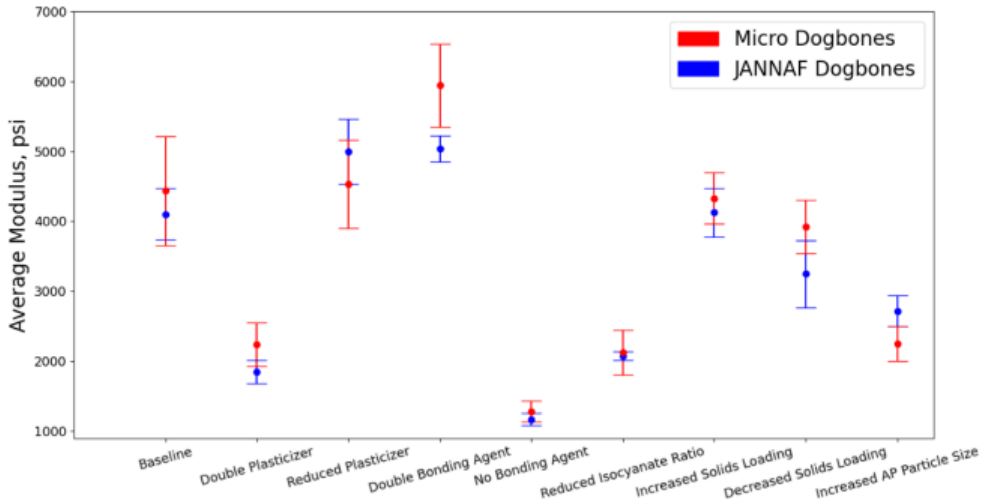

Figure 4-11. Distribution of Average Modulus Data Across All Formulations.

Table 4-2. Experimental Results from Uniaxial Tensile Tests.

Data Set	Mean Max Stress (psi)	Standard Deviation	Mean Strain at Max Stress (%)	Standard Deviation	Mean Modulus (psi)	Standard Deviation
Baseline						
JANNAF	131.00	2.00	3.94	0.35	4049.00	566.21
Micro	146.43	9.49	5.33	0.58	4433.86	776.51
Double Plasticizer (6% by wt.)						
JANNAF	96.25	4.92	8.63	1.75	1843.75	189.04
Micro	73.43	1.76	6.29	0.92	2239.14	312.63
Reduced Plasticizer (2% by wt.)						
JANNAF	155.25	8.38	4.41	0.66	4996.50	538.80
Micro	118.40	8.82	5.28	0.53	4531.80	627.29
Double Bonding Agent (0.5% by wt.)						
JANNAF	158.34	7.85	4.19	0.55	5042.25	215.58
Micro	173.12	4.16	3.95	0.40	5944.86	641.85
No Bonding Agent (0% by wt.)						
JANNAF	63.55	5.42	10.55	3.19	1169.75	101.20
Micro	61.08	6.85	8.22	1.07	1282.00	163.95
Reduced Isocyanate Ratio (0.75)						
JANNAF	103.00	1.41	9.56	0.11	2071.50	86.97
Micro	90.77	7.82	8.18	0.93	2122.69	333.56
Increased AP Particle Size (400 μm)						
JANNAF	133.33	3.79	7.36	0.58	2717.67	276.07
Micro	79.88	13.59	5.69	1.05	2252.00	264.24
Increased Solids Loading (87%)						
JANNAF	140.67	11.06	4.51	0.29	4126.00	426.27
Micro	134.00	8.74	4.83	0.70	4328.17	402.54
Decreased Solids Loading (83%)						
JANNAF	135.50	3.70	6.65	0.91	3247.50	550.93
Micro	128.67	5.65	6.66	0.89	3921.17	418.59

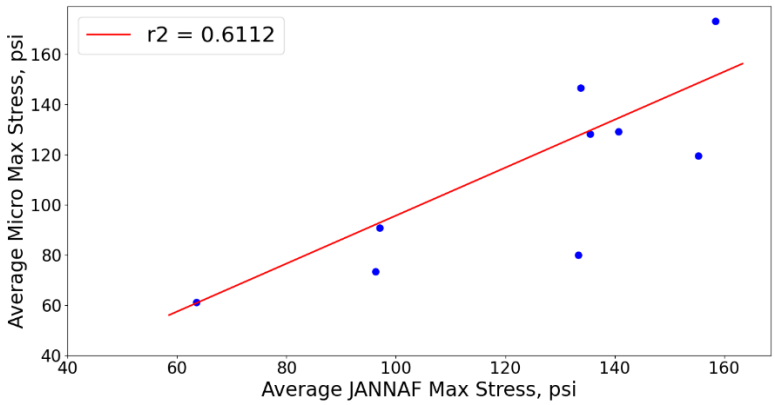

Figure 4-12. Micro vs JANNAF Dogbone Average Ultimate Stress Correlation.

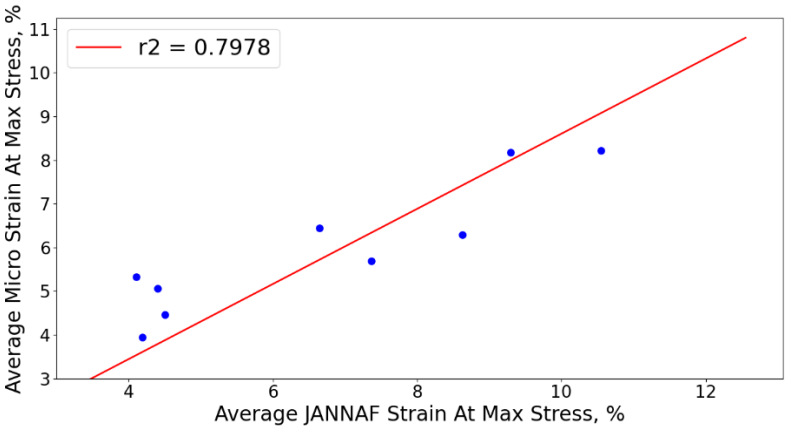

Figure 4-13. Micro vs JANNAF Dogbone Average Strain Correlation.

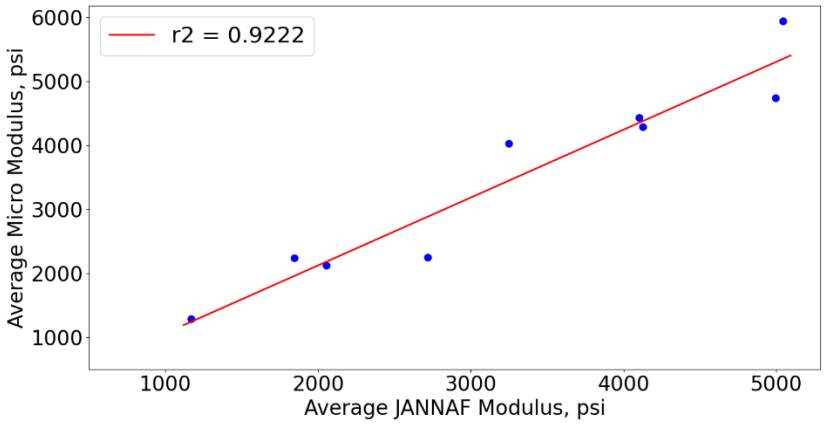

Figure 4-14. Micro vs JANNAF Dogbone Average Modulus Correlation.

From the stress-strain data, it can be observed that overall, there is not a strong correlation for max stress between the sample sizes, possibly owing to the effects of the size difference. The biggest outlier is observed to be the particle size difference, as seen in Figure 4-12, where the average stress between JANNAF and micro scales greatly lowers the R^2 value. Strain at max stress and Young's Modulus, however, do demonstrate stronger correlations. For practical applications, the micro dogbones would help determine the initial stiffness and strain capability of a propellant, before moving to large-scale testing for full characterization of strength, along with strain and stiffness.

4.3 Environmental Conditioning Results

In this portion of the experiments, propellant samples of both sizes were tested at -60 ^{o}C, -30 ^{o}C, 0 ^{o}C, and +60 ^{o}C to go along with the +25 ^{o}C (room temperature) tests previously performed. This allows for a broad analysis of both the material response to temperature changes and to observe if the micro-dogbones behave similarly to their JANNAF counterparts when at extreme temperatures.

Figure 4-15 below displays a representative depiction of the stress-strain graph of both JANNAF dogbones and micro-dogbones at -60 ^{o}C.

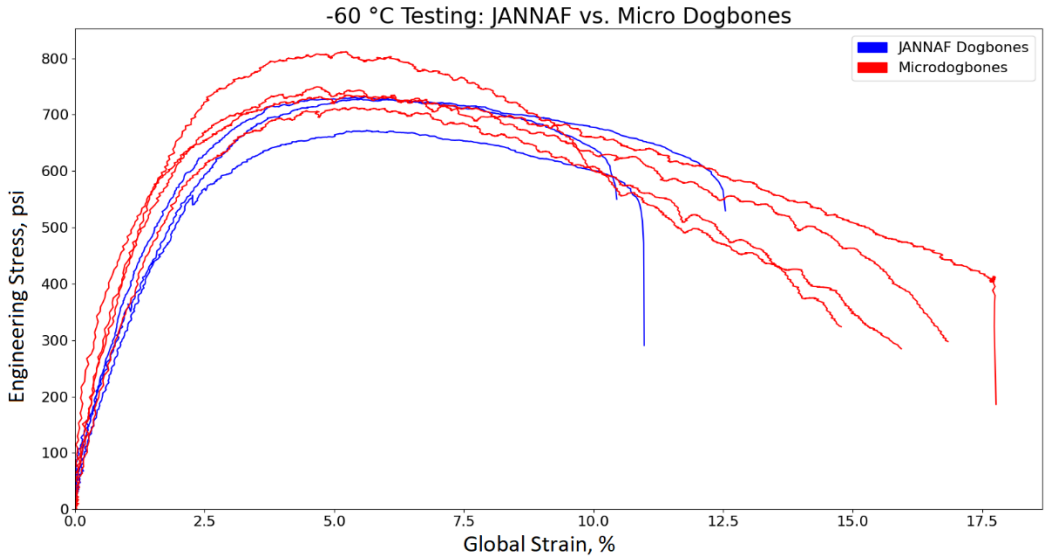

Figure 4-15. Stress-Strain Graph of Dogbones Tested at -60 °C.

As seen above, the two sample sizes track well together, even at an extreme end of the temperature range. Figure 4-16 and Figure 4-17 display the range of stress-strain behaviors for each sample size at each temperature.

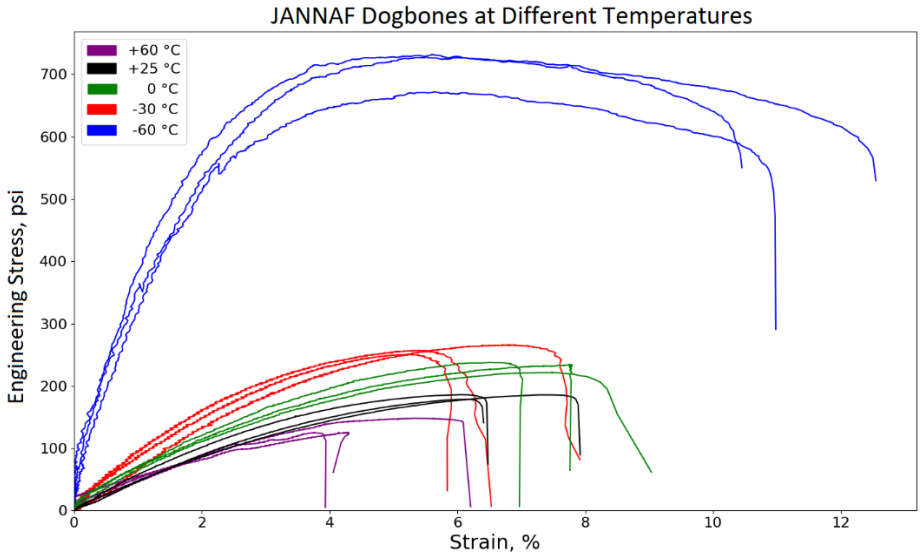

Figure 4-16. Stress-Strain Graph of JANNAF Dogbones in Temperature Testing Test Phase.

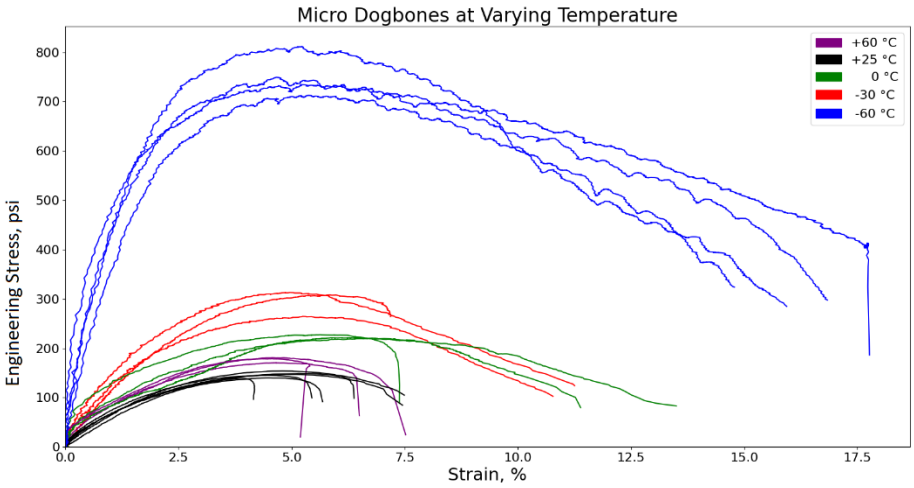

Figure 4-17. Stress-Strain Graph of Micro-dogbones in Temperature Testing Test Phase.

Within these results, it is clear to see how the modulus and maximum stress increase for both sample sizes as temperature decreases, which tracks with the expected results. The two sample sizes correlate strongly for modulus, as seen in Figure 4-18. Figure 4-19 and Figure 4-20 show similarly strong correlations for stress and strain, respectively. As before, the error bars are used more as a visual aid than strong statistical significance due to the limited sample size. At low temperatures, the micro-dogbones correlate to the JANNAF dogbones better than they do at higher temperatures, which provides another potential use for characterizing novel propellants with micro-dogbones over the JANNAF samples.

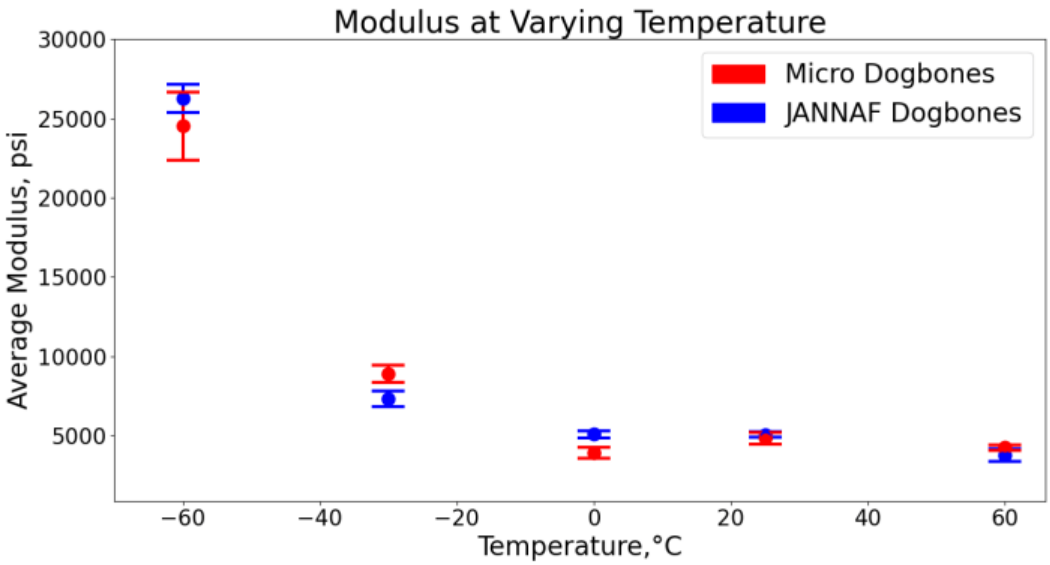

Figure 4-18. Representation of Correlation Between Sample Sizes for Young's Modulus During Temperature Testing.

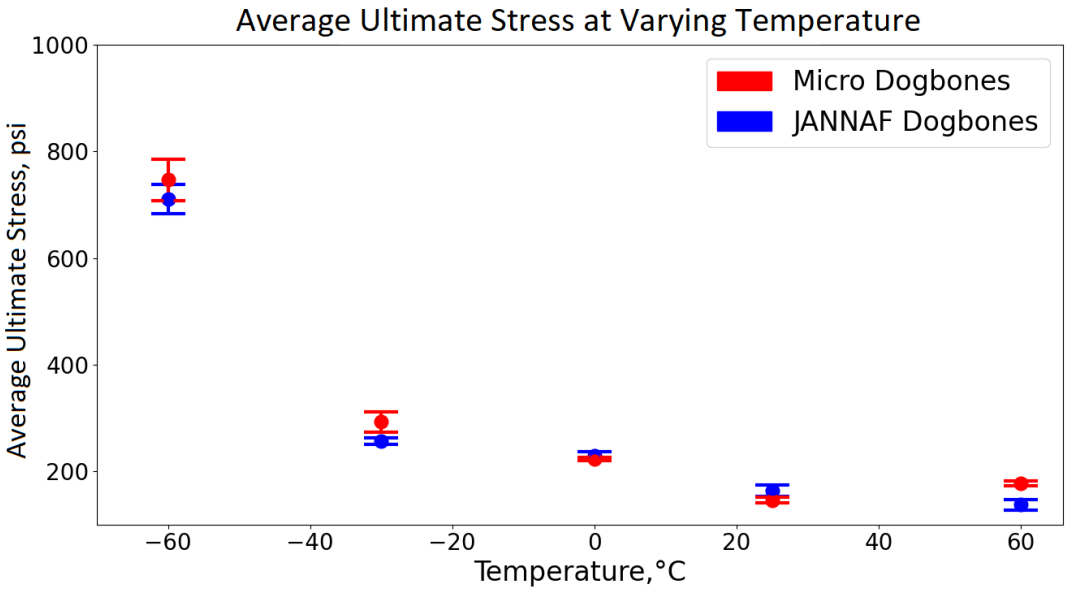

Figure 4-19. Representation of Correlation Between Sample Sizes for Ultimate Stress During Temperature Testing.

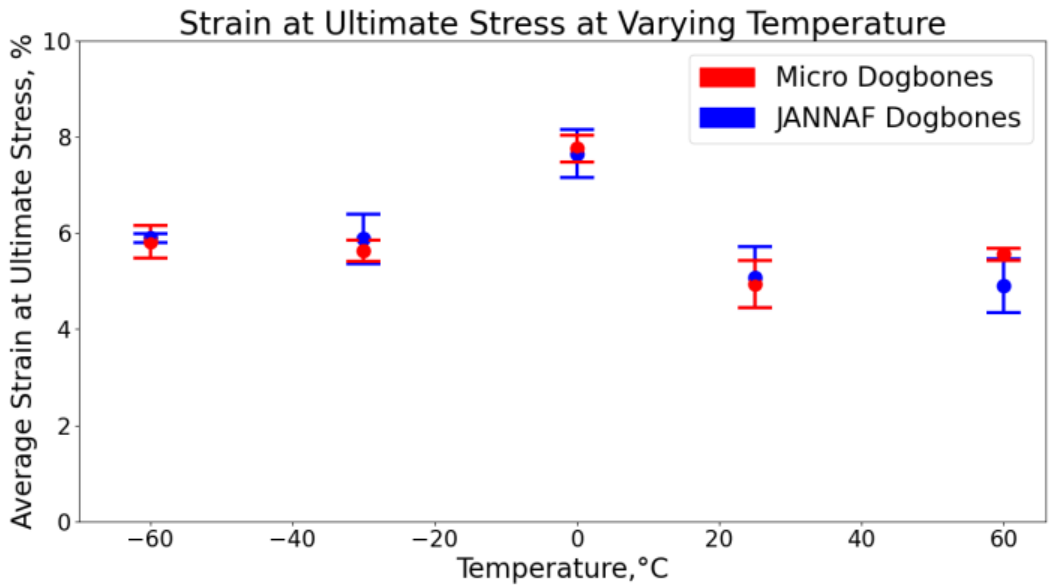

Figure 4-20. Representation of Correlation Between Sample Sizes for Strain at Ultimate Stress During Temperature Testing.

Using the same correlative method as before, the R^2 values for modulus, stress and strain throughout the temperature testing are 0.9909, 0.9906, and 0.8334, respectively. These micro-dogbones correlate strongly with the JANNAF dogbones across the temperature spectrum, supporting the idea that these smaller and easier to make samples could be used to help characterize novel solid propellants much faster than current industry methods.

Table 4-3. Temperature Testing Results Summary Table.

Data Set	Mean Max Stress (psi)	Standard Deviation	Mean Strain at Max Stress (%)	Standard Deviation	Mean Modulus (psi)	Standard Deviation
-60 °C						
JANNAF	710.33	27.18	5.90	0.09	26256.67	893.75
Micro	756.40	39.70	5.51	0.69	27289.60	5868.64
-30 °C						
JANNAF	256.00	6.36	5.88	0.52	7325.75	489.43
Micro	292.50	19.29	5.63	0.22	8914.50	521.50
0 °C						
JANNAF	228.75	7.40	7.66	0.50	5106.75	216.27
Micro	222.67	3.09	7.76	0.28	3923.00	346.22
25 °C						
JANNAF	163.25	10.47	5.08	0.63	5090.25	174.85
Micro	145.14	4.94	5.06	0.54	4707.57	473.65
60 °C						
JANNAF	137.00	9.98	4.90	0.55	3796.00	395.11
Micro	176.67	4.78	5.56	0.13	4272.67	172.26

4.4 Test Results Conclusion

Throughout each test campaign phase, promising results correlating the behavior of JANNAF and micro-dogbones were found, with modulus consistently having the strongest correlation. Additionally, the DIC system was used to great effect and demonstrated that faulty data could be quickly identified and discarded, reducing the overall test and analysis time. The void investigation displayed how the DIC system was able to distinguish between the samples with and without glass beads even if the beads are obscured from view, and how that behavior could be used to establish baseline behavior for samples that may contain voids. In the bead investigation, micro-dogbones containing an embedded glass bead were measured to have an average of 36% difference in local versus global strain, compared to an average value of 5% for samples without

a bead. Similarly, the JANNAF dogbones with an embedded glass bead displayed an 18% average difference for local versus global strain, while samples without the manufactured void had an average local versus global strain difference of just 5%.

As the formulations were changed, the micro-dogbones reflected similar trends to the JANNAF samples. Additionally, after varying the formulation composition to observe the effects on the mechanical properties of the propellant, the two sizes were found to have a good correlation in the Young's Modulus, maximum strain at ultimate stress, with R^2 values of 0.9222 and 0.7978, respectively. Maximum ultimate stress, however, was a more moderate correlation, with an R^2 value of 0.6112. The temperature changes introduced in the environmental testing reflected the ability of the micro-dogbones to display similar behavior to the JANNAF dogbones.

5. CONCLUSION

This work discusses the use of 2-D Digital Image Correlation (Digital Image Correlation) as a screening tool to help analyze and correlate the effect of changing propellant properties for different sample sizes. Tensile experiments of various propellant mixtures were tested successfully at both JANNAF and micro dogbone scales. During this, 2-D DIC was used to great effect in measuring the strain of each sample, providing a non-contact method of doing so.

Future work in this area could examine similar composite propellants, such as by using a different polymer or bonding agent. These could be changed to HTPB R45M and Tepanol with the effects on stress, strain, modulus, and embedded glass bead effects examined. New propellants would help determine if the mechanical properties differences in sample size are an artifact of the original propellant composition or if these differences are consistent across varied propellant types. Additionally, various strain rates could be examined, to determine the usefulness of the DIC system in high strain rate testing capacities. For the micro-dogbones, it would be useful to compare the results to an intermediate size between the JANNAF and micro scales to see how the correlations track with scaling, and if a slightly larger sample correlates more strongly to JANNAF-sized samples than the micro-dogbones.

Overall, the DIC system is a useful tool for non-contact strain measurement during tensile testing, and the micro dogbones display great for characterizing novel propellants faster, and at less cost, than current industry standards.

REFERENCES

[1] Mason, B. P., and C. M. Roland. “SOLID PROPELLANTS.” *Rubber Chemistry and Technology*, vol. 92, no. 1, Jan. 2019, pp. 1–24. *Silverchair*, https://doi.org/10.5254/rct.19.80456.

[2] “Solid-Propellant Rocket Motors.” *Solid-Propellant Rocket Motors - Proptools 0.0.0 Documentation*, https://proptools.readthedocs.io/en/latest/solid_tutorial.html.

[3] Sutton, George P, and Biblarz, Oscar. Rocket Propulsion Elements, 9th Edition. 9th ed. Wiley, 2017.

[4] Wibowo, Heri Budi, et al. *Rapid Analysis of HTPB (Hydroxyl Terminated Polybutadiene) Properties with Infrared Spectroscopy and Gel Chromatography*. 2020, p. 040012. *DOI.org (Crossref)*, https://doi.org/10.1063/5.0002819.

[5] “Historical Overview of HTPB the Military's Preferred Solid Propellant Binder for a Half Century.” *DSIAC*, https://dsiac.org/articles/historical-overview-of-htpb-the-militarys-preferred-solid-propellant-binder-for-a-half-century/.

[6] Kossakowski, Paweł. (2012). Influence of Initial Porosity on Strength Properties of S235JR Steel at Low Stress Triaxiality. Archives of Civil Engineering. 58. 293-308. 10.2478/v.10169-012-0017-9.

[7] Xin-guo, Liu et al. “Dewetting Stress of Solid Propellant under Tensile Loading.” 2018 9th International Conference on Mechanical and Aerospace Engineering (ICMAE) (2018): 570-573

[8] Guo, Jiahu, et al. “Kinetic Research on the Curing Reaction of Hydroxyl-Terminated Polybutadiene Based Polyurethane Binder System via FT-IR Measurements.” *Coatings*, vol. 8, no. 5, 5, May 2018, p. 175. *www.mdpi.com*, https://doi.org/10.3390/coatings8050175.

[9] Cui, Hui Ru, et al. “Study on the Viscoelastic Poisson‘s Ratio of Solid Propellants Using Digital Image Correlation Method.” *Propellants, Explosives, Pyrotechnics*, vol. 41, no. 5, 2016, pp. 835–43. *Wiley Online Library*, https://doi.org/10.1002/prep.201500313.

[10] Philipfigari, and Instructables. “Steps to Analyzing a Material's Properties from Its Stress/Strain Curve.” Instructables, Instructables, 10 Oct. 2017, https://www.instructables.com/Steps-to-Analyzing-a-Materials-Properties-from-its/.

[11] Rui, Shi, et al. “A Mesoscopic Damage Model of Solid Propellants under Thermo-Mechanical Coupling Loads.” *Polymer Testing*, vol. 79, Oct. 2019, p. 105927. *ScienceDirect*, https://doi.org/10.1016/j.polymertesting.2019.105927.

[12] Benedetto et. al. “In-Situ Tensile Testing of Propellants in SEM: Influence of

Temperature” Propellants Explos. Pyrotech. 2017, 42, 1396–1400. http://dx.doi.org/10.1002/prep.201700178

[13] van Ramshorst et. Al. « Investigation of the Failure Mechanism of HTPB/AP/Al Propellant by In-situ Uniaxial Tensile Experimentation in SEM” http://dx.doi.org/10.1002/prep.201500264

[14] Adel, Walid & †, H & El-Soualey, D. (2011). Experimental Determination of Some Design Properties of Viscoelastic Solid Propellant Using Uniaxial Tensile Test. 10.13140/RG.2.1.4625.3043.

[15] Bose, Partha & Pandey, Krishna. (2012). Desirability and Assessment of Mechanical Strength Characteristics of Solid Propellant for Use in Multi Barrel Rocket Launcher. International Journal of Chemical Engineering and Applications. 114-124. 10.7763/IJCEA.2012.V3.171.

[16] Wingborg, Niklas. “Increasing the Tensile Strength of HTPB with Different Isocyanates and Chain Extenders.” *Polymer Testing*, vol. 21, no. 3, Jan. 2002, pp. 283–87. *ScienceDirect*, https://doi.org/10.1016/S0142-9418(01)00083-6.

[17] Oberth, A.. (1967). Principle of Strength Reinforcement in Filled Rubbers. Rubber Chemistry and Technology. 40. 1337-1363. https://doi.org/10.5254/1.3539147.

[18] Gent, A. & Park, Byoungkyeu. (1984). Failure Processes in Elastomers at or Near a Rigid Spherical Inclusion. Journal of Materials Science. 19. 1947-1956. https://doi.org/10.1007/BF00550265.

[19] Toulemonde, Paul-Aymé, et al. “Effects of Small Particles on the Mechanical Behavior and on the Local Damage of Highly Filled Elastomers.” *Journal of Materials Science*, vol. 52, Jan. 2017, pp. 878–88. *ResearchGate*, https://doi.org/10.1007/s10853-016-0383-9.

[20] Ashish, Jauhari, et al. “Chapter 8 - Effect of Ammonium Perchlorate Particle Size on Flow, Ballistic, and Mechanical Properties of Composite Propellant.” *Nanomaterials in Rocket Propulsion Systems*, edited by Qi-Long Yan et al., Elsevier, 2019, pp. 299–362. *ScienceDirect*, https://doi.org/10.1016/B978-0-12-813908-0.00008-3.

[21] Aerojet- General. “Study of Mechanical Properties of Solid Rocket Propellant.” Report No. 041P1O1Q-1. **1961**

[22] El-Marsafy, Sahar. (2020). Effects of Bonding Agents, Curative Ratio and Burning Rate Modifiers on the Composite Polyurethane Studied by an Aging Program.

[23] Yadav, Anil & Pant, Chandra & Das, Sushanta. (2020). Research Advances in Bonding Agents for Composite Propellants. Propellants, Explosives, Pyrotechnics. 45. http://dx.doi.org/10.1002/prep.201900329

[24] Siviour, Clive & Gifford, M. & Walley, S.M. & Proud, W. & Field, J.. (2004). Particle size effects on the mechanical properties of a polymer bonded adhesive. Journal of Materials Science. 39. 1255-1258. https://doi.org/10.1023/B:JMSC.0000013883.45092.45

[25] Kundan Kumar, Arun Pooleery, K. Madhusoodanan, R.N. Singh, J.K. Chakravartty, B.K. Dutta, R.K. Sinha,Use of Miniature Tensile Specimen for Measurement of Mechanical Properties,Procedia Engineering,Volume 86,2014,Pages899-909,ISSN18777058, https://doi.org/10.1016/j.proeng.2014.11.112.

[26] G’Sell, C., Hiver, J., and Dahoun, A., Experimental Characterization of Deformation Damage in Solid Polymers under Tension, and Its Interrelation with Necking, Int. J. Solids Struct., vol. 39, nos. 13-14, pp. 3857–3872, 2002.

[27] Mohanraj, J., Barton, D., Ward, I., Dahoun, A., Hiver, J., and G’Sell, C., Plastic Deformation and Damage of Polyoxymethylene in the Large Strain Range at Elevated Temperatures, Polymer, vol. 47, no. 16, pp. 5852–5861, 2006.

[28] Ranjan, R., Murthy, H., Sadavarte, V., Pande, S., Bhowmik, D. AN EXPERIMENTAL STUDY OF THE LARGE-STRAIN TENSILE BEHAVIOR OF COMPOSITE SOLID PROPELLANT USING DIGITAL IMAGE CORRELATION.” *International Journal of Energetic Materials and Chemical Propulsion*, vol. 20, no. 4, 2021, pp. 79–95.

[29] T. C. Miller, Poisson's Ratio Extrapolation from Digital Image Correlation Experiments, Poisson's Ratio Extrapolation from Digital Image Correlation Experiments, AIR FORCE RESEARCH LAB EDWARDS AFB CA ROCKET PROPULSION DIV, 2013.

[30] Zhu, Daoli, et al. “Simultaneous Determination of Multiple Mechanical Parameters for a DNAN/HMX Melt-Cast Explosive by Brazilian Disc Test Combined with Digital Image Correlation Method.” *Propellants, Explosives, Pyrotechnics*, vol. 42, no. 8, 2017, pp. 864–72. *Wiley Online Library*, https://doi.org/10.1002/prep.201700010.

[31] Manship, Timothy D. *High Burn Rate Solid Composite Propellants*. Purdue University, 2010. *ProQuest*, https://www.proquest.com/docview/861341967/abstract/1C74B91C46944AF6PQ/1.